RAA 2018 Vol. **18** No. **1**, 6(14pp) doi: 10.1088/1674–4527/18/1/6

http://www.raa-journal.org *http://iopscience.iop.org/raa*

***R**esearch in*
***A**stronomy and*
***A**strophysics*

High energy properties of the flat spectrum radio quasar 4C 50.11

Jia-Neng Zhou[1], Vadakkumthani Jithesh[2,1], Liang Chen[1,3] and Zhong-Xiang Wang[1]

[1] Shanghai Astronomical Observatory, Chinese Academy of Sciences, Shanghai 200030, China; *zjn@shao.ac.cn*
[2] Inter-University Centre for Astronomy and Astrophysics, Post Bag 4, Ganeshkhind, Pune 411007, India
[3] University of Chinese Academy of Sciences, Beijing 100049, China

Received 2017 August 26; accepted 2017 October 22

Abstract We investigate the γ-ray and X-ray properties of the flat spectrum radio quasar (FSRQ) 4C 50.11 at redshift $z = 1.517$. The *Fermi*-LAT data indicate that this source was in an active state since July 2013. During this active period, the source's emission appeared harder in γ-rays, with the flux having increased by more than a factor of three. We analyze two distinct flares seen in the active state and find that the variability is as short as several hours. The *Swift*-XRT data show that the source was variable at X-ray energies, but no evidence is found for flux or spectral changes related to the γ-ray activity. The broad-band X-ray spectrum obtained with *Swift*-XRT and *NuSTAR* is described well by a broken power law model, with an extremely flat spectrum ($\Gamma_1 \sim 0.1$) below the break energy, $E_{\rm break} \sim 2.1\,{\rm keV}$, and $\Gamma_2 \sim 1.5$ above the break energy. The spectral flattening below $\sim 3\,{\rm keV}$ is likely due to the low energy cut-off in the energy distribution of the photon-emitting electron population. We fit the broad-band spectral energy distribution of the source during both the active and quiescent states. The X-ray and γ-ray emission from the jet is mainly due to the inverse-Compton scattering process, with seed photons provided from the broad line region, and the jet is estimated to be larger than the accretion power if the jet is mainly composed of electron-proton pairs.

Key words: galaxies: jets — gamma rays: galaxies — quasars: individual (4C 50.11) — radiation mechanisms: non-thermal

1 INTRODUCTION

Blazars are radio-loud active galactic nuclei (AGNs) with relativistic jets pointing towards the Earth (Blandford & Rees 1978). Because of the Doppler beaming effect, emission from a jet dominates the broad-band spectral energy distribution (SED) from radio to γ-ray energies (Urry & Padovani 1995). The SEDs usually have two broad bumps in a $\log\nu - \log\nu f_\nu$ diagram. While the low-energy bump usually peaks from infrared to X-ray energies, which are believed to be the synchrotron emission of non-thermal electrons, the high-energy bump peaks from X-ray to γ-ray bands, which is considered to be the inverse Compton (IC) emission of the same electron population. For IC emission, the seed photons can come from low-energy synchrotron emission, broad line region (BLR) or dusty torus (see e.g., Konigl 1981; Band & Grindlay 1985; Maraschi et al. 1992; Błażejowski et al. 2000). Because of the synchrotron self-absorption effect, blazars tend to have flat radio spectra with spectral index $\alpha < 0.5$. As a subclass of blazars, flat spectrum radio quasars (FSRQs) have strong optical emission lines (equivalent width > 5Å), compared to BL Lac objects that show no or very weak emission lines (Scarpa & Falomo 1997).

In the current third *Fermi* Large Area Telescope (LAT) source catalog (3FGL), the dominant extragalactic γ-ray sources are blazars (Acero et al. 2015). Extreme variability is not common to all blazars detected in γ-rays. The minimal variable timescale detected with *Fermi*-LAT has reached less than half an hour (e.g. PKS 1510-089, Foschini et al. 2013) and the variation amplitude can be two orders of magnitude (e.g., 3C 454.3; Abdo et al. 2011b). Detailed studies of spectra and vari-

abilities are essential for determining the location and mechanism of radiation from the jets of blazars.

FSRQ 4C 50.11 (also known as NRAO 150) is one of the strongest radio and millimeter AGN sources in the northern sky (Pauliny-Toth et al. 1966; Agudo et al. 2008, 2010). Very long baseline interferometry (VLBI) monitoring observations showed that the inner jet (inner 0.5 mas from the core) exhibits superluminal motions with $\beta_{\rm app} \sim (6.3 \pm 1.1)c$ and a large, $> 100^\circ$ projected misalignment of the jet within the inner 0.5 mas to 1 mas from the core (Agudo et al. 2007; Molina et al. 2014). These properties imply that a relativistic jet points toward the Earth with a very small viewing angle (Agudo et al. 2007). Acosta-Pulido et al. (2010) measured the redshift using near-infrared spectroscopic data (exhibiting strong Hα and Hβ emission lines), and derived the cosmological redshift $z = 1.517 \pm 0.002$, which corresponds to the luminosity distance $d_{\rm L} = 11.2 \times 10^3\,{\rm Mpc}$. Foschini (2010) reported the detection of γ-ray emission from 4C 50.11 with LAT on board the *Fermi* satellite. Using almost 20 months of data, he provided the γ-ray flux above 100 MeV, $F_{\rm 100MeV} = (3.2 \pm 1.1) \times 10^{-8}\,{\rm photons\,cm^{-2}\,s^{-1}}$, and photon index $\Gamma = 2.6 \pm 0.2$. After the γ-ray flaring activity around ∼MJD 56686 (2014 January 29), *Swift* target-of-opportunity observations were performed (Carpenter et al. 2014; Krauss et al. 2014).

For the purpose of fully studying this high-energy source, we collected its *Fermi*-LAT and available X-ray data, which include 15 *Swift* observations and one *NuSTAR* observation, and performed detailed analysis of the data. In this paper, we present the results from our analysis. In the following, Section 2 describes the data analysis of *Fermi*-LAT, *Swift* and *NuSTAR* observations. The obtained temporal and spectral results are presented in Section 3 and Section 4, respectively. We discuss the overall properties of the source in Section 5, including fitting to its multiwavelength SED, and we summarize our results in Section 6.

2 DATA REDUCTION

2.1 *Fermi*-LAT Data Analysis

We used approximately seven-years of *Fermi*-LAT Pass 8 data in this work, which are from MJD 54682 (2008–08–04) to MJD 57352 (2015–11–26), with energy range from 100 MeV to 100 GeV. During the time period, 4C 50.11 was in an active state from MJD 56482 (2013–07–09) to the end of the data. The Fermi Science Tools v10r0p5 package was used to analyze the data, with the `P8R2_SOURCE_V6` instrument response functions (IRFs) applied. To avoid contamination from γ-rays reflected by the Earth, we selected the events with zenith angles $\leq 90^\circ$.

In the analysis, photons from a $20^\circ \times 20^\circ$ square region of interest (ROI) centerd at the position of 4C 50.11 were selected, and binned into spatial pixels of $0.1^\circ \times 0.1^\circ$. The first run of the analysis, using `gtlike`, was performed with the binned likelihood method to derive the sky map model. We modeled the events considering the components of the target and background. The background was composed of sources in the 3FGL catalog (Acero et al. 2015) within the ROI and diffuse components. The latter included the Galactic diffuse model (`gll_iem_v06.fits`) and isotropic background (`iso_P8R2_SOURCE_V6_v06.txt`).

To confirm the spatial association of γ-ray emission with 4C 50.11, we calculated a $2^\circ \times 2^\circ$ Test Statistic (TS) map centered at its coordinates. A putative point source was assumed and moved through a grid of locations on the sky by maximizing $-\log$(likelihood) at each grid point. In this step, the target source that corresponded to 4C 50.11 was unmodeled (i.e., removed from the model file). All parameters of point sources in the ROI, except the diffuse components, were fixed at the 3FGL catalog values. To reduce contamination due to the large point spread function (PSF) at low energies, we only used photons above 1 GeV for TS map calculation. The γ-ray source was significantly detected, with a maximum TS value of $\simeq 283$. We derived the position of the source, and the best-fit position is RA = 59.872°, Decl. = 50.968° (J2000.0) with a positional uncertainty of 0.022°. The derived position is only $0.25'$ away from 4C 50.11.

Since 4C 50.11 is located on the Galactic plane ($b = -1.6^\circ$; Fey et al. 2004), we checked the SIMBAD database for sources within the error circle. There are only a few sources cataloged by 2MASS and SDSS (a ROSAT source 1RXS J035930.6+505730 is also within the error circle, but it has been considered as the likely counterpart to 4C 50.11; Agudo et al. 2007). The nearest source is located at a distance of 3.6° (Acero et al. 2015). In addition, since the γ-ray background can be complex at the Galactic plane, we also checked the normalization value for the Galactic diffuse emission. It was 0.963 ± 0.003. Considering the systematic uncertainty of

6% for the background (Abdo et al. 2013, 2010b), the value is consistent with the expected normalization of 1.

2.2 *Swift* Data Analysis

The *Swift* satellite (Gehrels et al. 2004) performed 15 observations of 4C 50.11 between January 2007 and December 2015. We utilized archival data from the X-ray telescope (XRT; Burrows et al. 2005) on board *Swift*. The XRT data were processed with standard filtering and screening criteria, using the XRTPIPELINE version 0.13.0 in the HEASOFT package version 6.15.1. The photon-counting (PC) mode data were collected from all the observations. Since the source had low count rates ($< 0.1\,\mathrm{counts\,s^{-1}}$), pile-up correction was not required. Source events were extracted from a circular region with a radius of $47''$, while background events were extracted from a circular region of the same radius, with the standard grade filtering of 0–12. We generated the ancillary response files with the tool XRTMKARF and used spectral redistribution matrices available in the calibration database (CALDB) version 20151105. The spectra were binned to contain at least 20 counts per bin, which allowed χ^2 spectral fitting. In other cases, where there were no sufficient spectral counts, the Cash Statistic (Cash 1979) was used for spectral modeling.

2.3 *NuSTAR* Data Analysis

NuSTAR (Harrison et al. 2013) observed 4C 50.11 with its focal plane module A (FPMA) and B (FPMB) X-ray telescopes, on 2015 December 14 for an exposure time of 20.5 ks (Observation ID: 60160177002). We processed the data with the *NuSTAR* Data Analysis Software NUSTARDAS version 1.3.1. We cleaned and calibrated the unfiltered event files using standard filtering criteria with the NUPIPELINE task and *NuSTAR* CALDB version 20151008. The source and background regions were taken from a circular region of radius $70''$, and we generated the spectra, response matrices and ancillary response files, using NUPRODUCTS for both focal plane modules (FPMA and FPMB). The *NuSTAR* FPMA and FPMB spectra were grouped with a minimum of 20 counts per bin using HEASOFT task GRPPHA. We did not combine the spectra from FPMA and FPMB; instead we jointly fitted the two spectra.

3 VARIABILITY IN γ-RAY AND X-RAY

3.1 γ-ray Temporal Properties

Since 4C 50.11 was active from $\sim$MJD 56482, showing γ-ray flares, a 5-day binned light curve was derived using the binned likelihood method. Normalizations of all point sources within 5° from the target and sources with variable index[1] $\geq$72.44 were set free. For the purpose of studying the flaring variability in detail, 24-, 12- and 6-hour binned light curves were also created. For these light curves, an unbinned likelihood method was used due to the low statistics, and only the normalizations of variable sources were set free in the background model. In the analysis, when a data point had TS$<$5, we calculated its flux upper limit at a 95% confidence level (Abdo et al. 2011a).

Figure 1 shows the γ-ray light curves of 4C 50.11 in 0.1–100 GeV, with the upper panel covering the entire *Fermi* observation time period (setting 30 day time bins) and the lower panel covering the γ-ray active period starting from $\sim$MJD 54682. Six time intervals are shown based on the light curves (see Fig. 1): P1 is the time period before the active state and P2–P6 the time periods covering the active state, which lasts for more than two years. Examining the light curves, there are two distinct γ-ray flares in the active state, P3 and P5, which appear to contain several data points above the nearby flux levels and have peak fluxes more than two times higher. We thus obtained smoothed 5-day light curves (by shifting each time bin by 1 day) for them and determined their approximate time durations (marked by the grey area in Fig. 2). Detailed analysis of the peak regions of the two flares is provided below.

We investigated the active state of 4C 50.11 in different energy bands. The two flaring events (P3 and P5) are clearly seen in the 0.1–1 GeV energy band (Fig. 2). However in the >1 GeV energy light curve, the flares do not have significantly higher flux than the rest of the light curve, and the overall photon flux is an order of magnitude lower than that in the 0.1–1 GeV energy band.

We modeled the photons in each 5-day time bin with a single power law (PL) model because of the low counts of the data points (see below for detailed discussion about spectral modeling in Sect. 4.1). As shown in the bottom panel of Figure 2, the derived photon index varies with time and flux. However no obvious trend can

[1] *http://fermi.gsfc.nasa.gov/ssc/data/access/lat/4yr_catalog/*

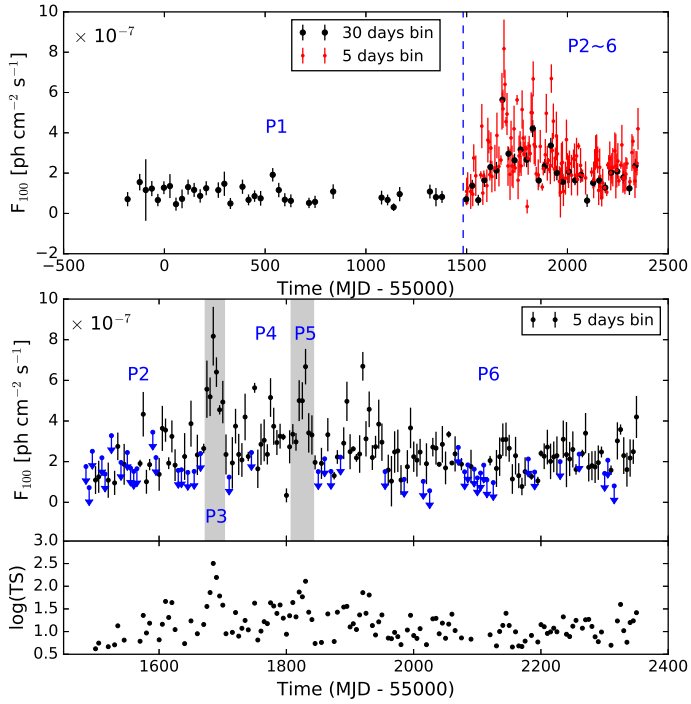

Fig. 1 *Fermi*-LAT light curves of 4C 50.11 with energy between 100 MeV and 100 GeV. Different time intervals are shown based on the light curve properties. *Upper:* Long-term light curves binned with 30 d (*black points*) and 5 d (*red points*). *Lower:* 5-day binned light curve of 4C 50.11 during the γ-ray active period from MJD 56482, and $\log(\mathrm{TS})$ values for each bin. When TS < 5, only flux upper limits (95% confidence) are obtained.

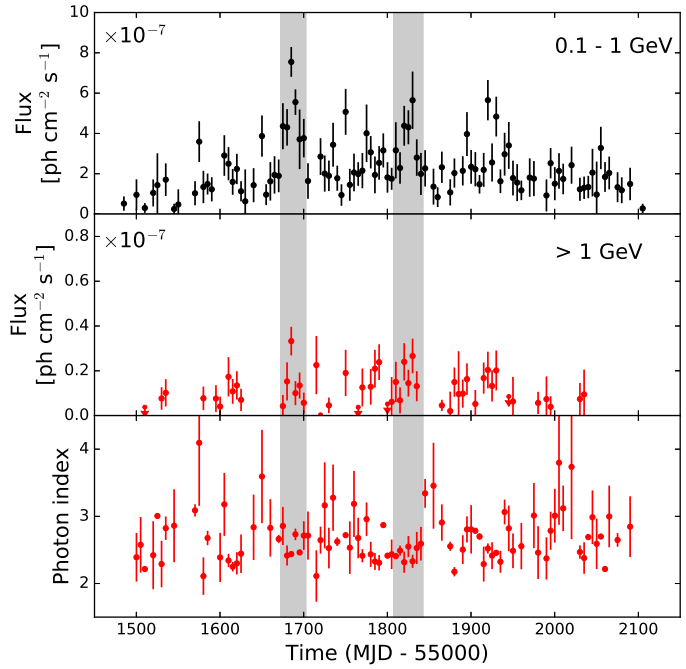

Fig. 2 Five-day binned light curves of 4C 50.11 observed by *Fermi*-LAT during the γ-ray active period. From *top* to *bottom*: light curve at 0.1–1 GeV band, that at the 1–100 GeV band and photon index obtained from a PL model. The *shaded area* indicates γ-ray flares P3 and P5.

Table 1 Fitting Results for the Peaks in Flares P3 and P5

Flare	$F_{\rm c}$ ($\times10^{-7}$)	F_0 ($\times10^{-7}$)	t_0 (MJD)	$\tau_{\rm r}$ (h)	$\tau_{\rm d}$ (h)
P3	1.3±0.3	22.6±0.4	56687.27±0.73	40.1±1.4	22.3±0.5
P5	4.3±0.3	28.2±1.4	56831.26±0.04	11.9±0.9	3.5±1.1

Notes: $F_{\rm c}$ and F_0 are in units of $\rm ph\,cm^{-2}\,s^{-1}$.

be drawn from the variations, as the photon index generally has values in a range of 2–3.

The peak regions of the two flares are shown in Figure 3. The first one started at ∼MJD 56685 and lasted for ∼5 d. During this period, the profile is relatively flat, while a small sub-flare around MJD 56690 is seen, which lasted only ∼2 d. We extracted the spectrum of the peak region and fitted it with a single PL model. From fitting, we found averaged photon flux $F_{100\,\rm MeV} = (6.3 \pm 0.3) \times 10^{-7}\,\rm photons\,cm^{-2}\,s^{-1}$ and photon index $\Gamma = 2.55 \pm 0.04$. In the second flare, the peak is around ∼MJD 56831, which has a different shape compared to that of the first one. The averaged photon flux of this flare was $F_{100\,\rm MeV} = (4.6 \pm 0.3) \times 10^{-7}\,\rm photons\,cm^{-2}\,s^{-1}$ and photon index $\Gamma = 2.44 \pm 0.05$. The peak flux (given from the 6-hour light curves) was $(2.0 \pm 0.5) \times 10^{-6}\,\rm photons\,cm^{-2}\,s^{-1}$. We studied the two peaks by fitting their light curves with equation (7) in Abdo et al. (2010c),

$$F(t) = F_{\rm c} + F_0\Big[e^{(t_0-t)/\tau_{\rm r}} + e^{(t-t_0)/\tau_{\rm d}}\Big]^{-1} \quad , \quad (1)$$

which is widely used to characterize a variation profile (see e.g. Hayashida et al. 2015). In this function, $F_{\rm c}$ and F_0 are the underlying constant level and flare amplitude, respectively, t_0 approximately corresponds to the flux peak time (when a flare has a symmetric shape), and rise time $\tau_{\rm r}$ and decay time $\tau_{\rm d}$ characterize the timescales for the rising and decaying parts of a flare. We chose to fit the peaks in the middle panels of Figure 3, which are significant and are relatively well resolved. The fitting results are listed in Table 1. The two peaks in P3 and P5 show asymmetric profiles, with a minimum timescale in P5 as short as ∼4 h.

3.2 X-ray Temporal Properties

The obtained long-term *Swift*-XRT count-rate curve of 4C 50.11 is shown in Figure 4. During the years 2007–2015, the source showed variability with count rates varying by a factor of ∼ 3. We also observed an increase of the count rate in the latest *Swift*-XRT observations and it reached the maximum value of ∼ $0.08\,\rm counts\,s^{-1}$ on 2015 December 14. Since the γ-ray analysis points to hour-scale variability of the source, we checked the longest *Swift*-XRT observation (conducted on 2007 December 2), but did not find any evidence for such variability in light curves binned at different half-hourly or hourly timescales.

4 SPECTRAL PROPERTIES

4.1 Spectral Properties in γ-ray Band

We analyzed the γ-ray spectra of 4C 50.11 in the different time intervals (P1–P6) and the total time interval of the combined P2–P6. Models of simple PL ($dN/dE \propto E^{-\Gamma}$), broken PL (BPL; $dN/dE \propto E^{-\Gamma_1}$ for $E < E_{\rm break}$, and $dN/dE \propto E^{-\Gamma_2}$ for $E > E_{\rm break}$), and log-parabola ($dN/dE \propto (E/E_b)^{-\alpha-\beta\log(E/E_b)}$) were considered. The results are given in Table 2. The three models generally describe the spectrum well, as indicated by the obtained TS values that are nearly the same. However for the total time interval of P2–P6, the active state, the BPL and log-parabola models are probably more favored than the single PL.

In Figure 5, we show the spectrum from the combined P2–P6 data and the three model fits. The PL fit does not describe the high energy tail of the spectrum as well as the two other models, which is also supported by values of likelihood ratio $-2\Delta L$ (see Table 2).

From the analysis, one property may be drawn if we consider the results from the PL fits or BPL fits: emission from the source appears harder when brighter (see Table 2). However, the uncertainties are too large, not allowing us to draw a clear conclusion. In any case, it is certain that emission in the active state is harder than that in quiescence.

4.2 Spectral Properties in X-ray Band

We fitted 15 *Swift*-XRT spectra with an absorbed PL model in the $0.3 - 10\,\rm keV$ energy band. The absorption was incorporated by using the photoelectric absorption model `tbabs` (Wilms et al. 2000), which was fixed at the Galactic value, $6.93 \times 10^{21}\ \rm cm^{-2}$ (Kalberla et al. 2005). The results are reported in Table 3. All errors are given at the 90% confidence level.

For four observations, conducted on 2007 November 5 (Obs ID: 00036308001), 2007 December 2 (Obs ID: 00036308002), 2008 October 24 (Obs ID: 00036308005) and 2015 December 14 (Obs ID: 00080948001), there are enough spectral counts to test other spectral models.

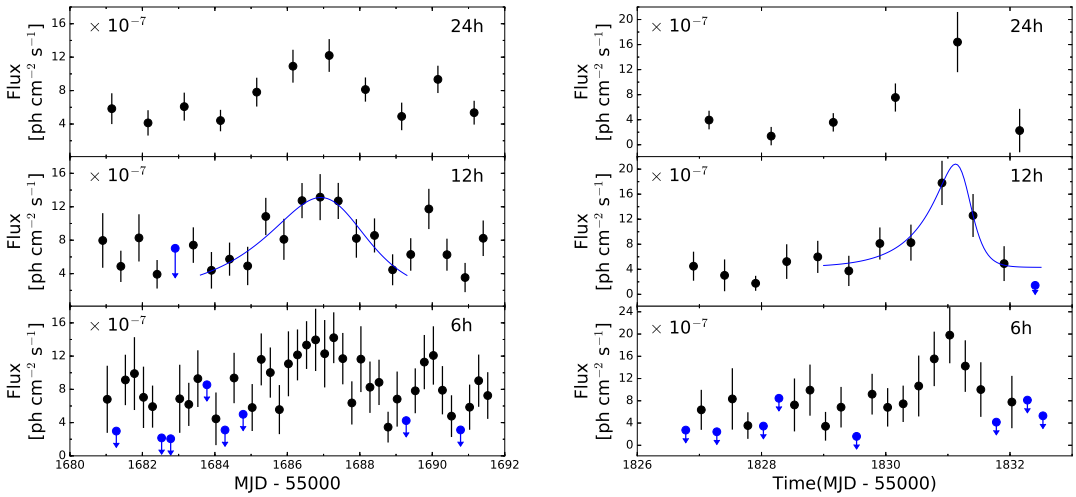

Fig. 3 Light curves of the peak regions in flares P3 (*left*) and P5 (*right*). From *top* to *bottom*: the light curves binned with 24, 12 and 6 hours, respectively. For points with TS < 5, upper limits are calculated at a 95% confidence level. The curves in the *middle panels* are the fits to the flux variations.

Table 2 γ-ray Spectral Fitting Results for 4C 50.11 in Different Time Intervals

Interval	Model	$\alpha/\Gamma/\Gamma_1$	β/Γ_2	$E_{\rm break}$ (GeV)	TS	$-2\Delta L$	Flux (10^{-7})
	PL	3.01±0.03	...	...	303	...	(6.99±0.35)E–1
P1	LogP	3.01±0.08	0.00±0.00	...	304	0.0	(6.99±0.48)E–1
	BPL	2.97±0.17	3.15±0.77	1.0±0.1	303	0.2	(6.94±0.45)E–1
	PL	2.63±0.07	...	...	234	...	1.65±0.15
P2	LogP	2.23±0.13	0.18±0.06	...	236	6.4	1.50±0.15
	BPL	2.38±0.11	3.30±0.43	1.0±0.3	237	6.8	1.52±0.16
	PL	2.55±0.04	...	...	654	...	6.30±0.30
P3	LogP	2.42±0.10	0.06±0.04	...	651	3.8	6.14±0.39
	BPL	2.44±0.08	2.87±0.24	1.0±0.2	652	5.0	6.11±0.39
	PL	2.61±0.06	...	...	347	...	2.87±0.21
P4	LogP	2.17±0.13	0.22±0.06	...	304	10.6	2.63±0.21
	BPL	2.37±0.09	3.40±0.47	1.0±0.3	303	9.2	2.69±0.22
	PL	2.44±0.05	...	...	358	...	4.59±0.28
P5	LogP	2.22±0.08	0.10±0.03	...	359	2.4	4.37±0.29
	BPL	2.26±0.07	2.90±0.22	1.0±0.0	361	3.8	4.35±0.34
	PL	2.69±0.05	...	...	504	...	2.10±0.12
P6	LogP	2.51±0.09	0.08±0.04	...	503	3.2	2.03±0.13
	BPL	2.58±0.07	2.97±0.21	1.0±0.2	504	2.6	2.05±0.13
	PL	2.63±0.02	...	...	2175	...	2.38±0.07
P2–P6	LogP	2.35±0.05	0.14±0.02	...	2180	32.2	2.24±0.07
	BPL	2.45±0.04	3.29±0.17	1.2±0.1	2191	36.4	2.26±0.07

Notes: Flux (0.1–100 GeV) is in units of ph cm^{-2} s^{-1}. $-2\Delta L$ is the difference in log(Likelihood) of the model with respect to that of the single PL model (e.g., Abdo et al. 2010a).

We initially added an extra absorption component at the redshift of the source (`ztbabs`) to the PL model. This combined model improved the spectral fit for three observations (with $\Delta\chi^2 \sim 7-9$) for the loss of one degree of freedom (d.o.f) over the single PL. For the remaining one (2008 October 24), the spectral fit was marginally improved, $\Delta\chi^2 \sim 2$. In order to determine the significance of the added extra absorption component, we sim-

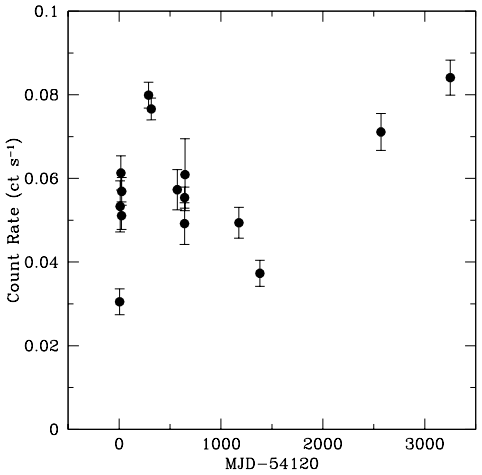

Fig. 4 Count rate variations of 4C 50.11 seen in the *Swift*-XRT observations over the years 2007–2015.

Table 3 *Swift*-XRT Observations of 4C 50.11 and the Fitting Results using a PL Model with $N_{\rm H}$ Fixed to the Galactic Absorption

ObsID	Date	Exposure time (s)	$\Gamma_{\rm X}$	$0.3-10$ keV Flux (10^{-12} erg cm^{-2} s^{-1})	χ^2/d.o.f
(1)	(2)	(3)	(4)	(5)	(6)
00030879001	2007 Jan 25	3505	$0.76^{+0.44}_{-0.44}$	$5.36^{+1.75}_{-1.23}$	7.6/7(C)
00030879002	2007 Jan 30	1513	$1.46^{+0.47}_{-0.47}$	$6.65^{+1.42}_{-1.24}$	5.6/12(C)
00030879003	2007 Feb 07	3845	$1.00^{+0.28}_{-0.28}$	$8.06^{+1.27}_{-1.14}$	3.0/8
00030879004	2007 Feb 13	5329	$1.17^{+0.27}_{-0.27}$	$6.38^{+0.86}_{-0.81}$	3.2/8
00030879005	2007 Feb 15	5276	$1.16^{+0.24}_{-0.24}$	$6.48^{+0.78}_{-0.74}$	9.0/11
00036308001	2007 Nov 05	8778	$1.20^{+0.13}_{-0.13}$	$8.47^{+0.63}_{-0.62}$	34.0/30
00036308002	2007 Dec 02	11952	$1.05^{+0.11}_{-0.11}$	$9.02^{+0.61}_{-0.59}$	49.6/40
00036308003	2008 Aug 13	2612	$0.83^{+0.35}_{-0.36}$	$7.99^{+1.94}_{-1.43}$	11.1/11(C)
00036308004	2008 Oct 23	2173	$1.17^{+0.52}_{-0.51}$	$7.02^{+2.05}_{-1.37}$	14.4/7(C)
00036308005	2008 Oct 24	9514	$1.10^{+0.14}_{-0.14}$	$7.10^{+0.61}_{-0.59}$	18.7/23
00036308006	2008 Oct 27	873	$0.80^{+0.71}_{-0.71}$	$8.79^{+3.59}_{-2.30}$	3.3/7(C)
00030879006	2010 Apr 10	3780	$0.82^{+0.29}_{-0.29}$	$6.70^{+1.40}_{-1.09}$	6.1/15(C)
00030879007	2010 Nov 01	3930	$0.96^{+0.36}_{-0.36}$	$6.06^{+1.36}_{-1.01}$	8.5/11(C)
00036308007	2014 Feb 02	3854	$1.14^{+0.23}_{-0.23}$	$8.27^{+1.04}_{-0.99}$	9.3/10
00080948001	2015 Dec 14	5011	$1.25^{+0.17}_{-0.17}$	$9.08^{+0.87}_{-0.85}$	27.5/17

Notes: (1) Observation ID used for the analysis; (2) date of observation; (3) exposure time in seconds for each observation; (4) photon index; (5) unabsorbed flux in $0.3-10$ keV band derived using `cflux` model; (6) the χ^2/d.o.f value for the model, where C-statistics are indicated by C.

ulated 1000 spectra using the Monte Carlo method with the XSPEC tool *simftest* and fit them with the absorbed PL and PL plus extra absorption models. An analysis of F-test probability using this method suggests that the significance of the extra component is $2.8-3.3\sigma$ in the three observations, while the significance is lower ($\sim 1.6\sigma$) in the observation conducted on 2008 October 24. The extra absorption at the redshift of the source ($N_{\rm H}^z$) is in a range of $6.5-12.6\times10^{22}\,{\rm cm}^{-2}$ for these four observations.

We also considered a broken PL model for all the four observations. For the November 2007 observation, the broken PL fit resulted in $\Gamma_1 < 0.99$ below the break energy $E_{\rm break} = 2.56^{+0.58}_{-1.23}$ keV and $\Gamma_2 = 1.68^{+0.36}_{-0.42}$ above the break energy, (χ^2/d.o.f = 24.8/28). For the December 2007 observation, the broken PL provided an acceptable fit with $\Gamma_1 = 0.12^{+0.58}_{-0.70}$, $E_{\rm break} = 2.08^{+0.61}_{-0.24}$ keV and $\Gamma_2 = 1.35^{+0.20}_{-0.19}$ (χ^2/d.o.f = 38.9/38). The photon index $\Gamma_1 = -0.31^{+1.10}_{-1.20}$,

$E_{\rm break} = 2.18^{+0.91}_{-0.25}$ keV and $\Gamma_2 = 1.80^{+0.59}_{-0.33}$ were obtained for the observation in 2015 (χ^2/d.o.f = 15.8/15). This model provided an improvement to the spectral fit for the three observations, with $\Delta\chi^2 \sim 9-11$ for the loss of two extra d.o.fs at a probability of $> 98\%$ (from F-test), over the single PL fit. The F-test results suggest that the broken PL is the best-fit spectral model for the source. However for the October 2008 observation, the broken PL model provides a marginally improved spectral fit (at a probability of $< 80\%$) over the single PL. Moreover, the break energy obtained ($E_{\rm break} \sim 3.26$ keV) in this observation was not well constrained. We thus fixed $E_{\rm break}$ at 3.26 keV, which yielded $\Gamma_1 = 0.85^{+0.29}_{-0.31}$ and $\Gamma_2 = 1.47^{+0.44}_{-0.41}$ (χ^2/d.o.f = 16.1/22).

We noted that in Foschini (2009), an exponential roll-off component was used to describe the low-energy part of a spectrum (< 2 keV) when the spectrum could not be fit well with a broken PL. We tested the model by adding the roll-off component (`expabs`) to a PL. This model improved the spectral fit over the single PL, but was worse compared to the models of the extra absorption plus PL or the broken PL in all the four cases. This was also true for our fit to the joint *NuSTAR* and *Swift*-XRT spectrum (see Table 4).

The *Swift* Burst Alert Telescope (BAT; Barthelmy et al. 2005) observed the source with short-exposure observations, where the hard X-ray flux of the source was below the sensitivity of the BAT instrument. Therefore no BAT analysis was conducted here. However the source is included in the *Swift*-BAT 70-month hard X-ray catalog (Baumgartner et al. 2013). The reported results of the hard X-ray spectrum (14–195 keV energy range) were a PL with photon index $\Gamma_{\rm X} = 1.51 \pm 0.35$ and a flux of $1.99^{+0.55}_{-0.51} \times 10^{-11}\,{\rm erg\,cm^{-2}\,s^{-1}}$.

The *NuSTAR* spectra in the 3–79 keV energy range were fitted with an absorbed PL model, where the absorption was fixed at the Galactic value. The fit yielded photon index $\Gamma_{\rm X} = 1.52 \pm 0.04$, an unabsorbed flux (derived using `cflux` model) of $(3.05 \pm 0.14) \times 10^{-11}\,{\rm erg\,cm^{-2}\,s^{-1}}$, with χ^2/d.o.f = 342.8/390. The photon index obtained with the absorbed PL model is the same as Γ_2 obtained from the broken PL model for the joint *NuSTAR* and *Swift*-XRT spectra in the $0.3-79$ keV energy range. We also searched for any hourly variability in the *NuSTAR* data, but no apparent variations were found.

The simultaneous observations of 4C 50.11 with *NuSTAR* and *Swift*-XRT were performed on 2015 December 14. We thus studied the X-ray spectrum of 4C 50.11 over the wide energy range of $0.3-79$ keV. The broad-band spectrum was fitted with a PL, a PL plus extra absorption component, a PL plus exponential roll-off and a broken PL. In all models, the absorption component (`tbabs`) was fixed at the Galactic value. The best-fit spectral parameters obtained from the simultaneous fitting are given in Table 4. The cross-calibration uncertainties between the three telescopes (*NuSTAR* FPMA, FPMB and *Swift*-XRT) were considered by adding a multiplicative constant in the model, which was frozen at 1 for the FPMA spectrum and free to vary for the FPMB and XRT spectra. The PL model provided an acceptable fit for the joint spectrum with $\Gamma_{\rm X} = 1.51^{+0.04}_{-0.03}$ and χ^2/d.o.f = 373.1/407, while the addition of an extra absorption at the redshift of the source improved the fit by $\Delta\chi^2 \sim 9$ for the loss of one extra d.o.f (significance of the extra component is $\sim 2.9\sigma$). The extra absorption column density obtained by this fit is $5.47^{+3.50}_{-3.10} \times 10^{22}\,{\rm cm^{-2}}$. The PL plus exponential roll-off model for the broad-band spectrum was marginally as good as the PL plus extra absorption component (χ^2/d.o.f $= 366.7/406$; see Table 4). The broken PL model further improved the spectral fit compared to the PL plus the extra absorption model and PL plus exponential roll-off model. The spectrum and model fit are shown in Figure 6. The difference in the cross-calibration between FPMA and FPMB was $< 4\%$ in all models, while for the XRT spectrum it was slightly larger but always less than 13%. This difference became larger ($\sim 23\%$) when a single PL model was used.

5 DISCUSSION

5.1 Gamma-ray Properties

We have studied the γ-ray properties of 4C 50.11 by analyzing the *Fermi*-LAT data, and confirmed the prediction in Acosta-Pulido et al. (2010) that 4C 50.11 is a luminous γ-ray emitter. The observed γ-ray photon index of 4C 50.11 has a range of $\Gamma \approx 2.4-3.0$ (see Table 2), which is roughly consistent with that of *Fermi*-LAT γ-ray FSRQs ($\langle\Gamma\rangle \approx 2.4-2.5$; Ackermann et al. 2015). From the temporal analysis, we found that 4C 50.11 has been in an active state since July 2013. During the active period, the γ-ray flux increased by > 3 times compared to the quiescence level and the emission was harder. Moreover, two distinct γ-ray flares were clearly seen in the $0.1-1$ GeV light curve during this period.

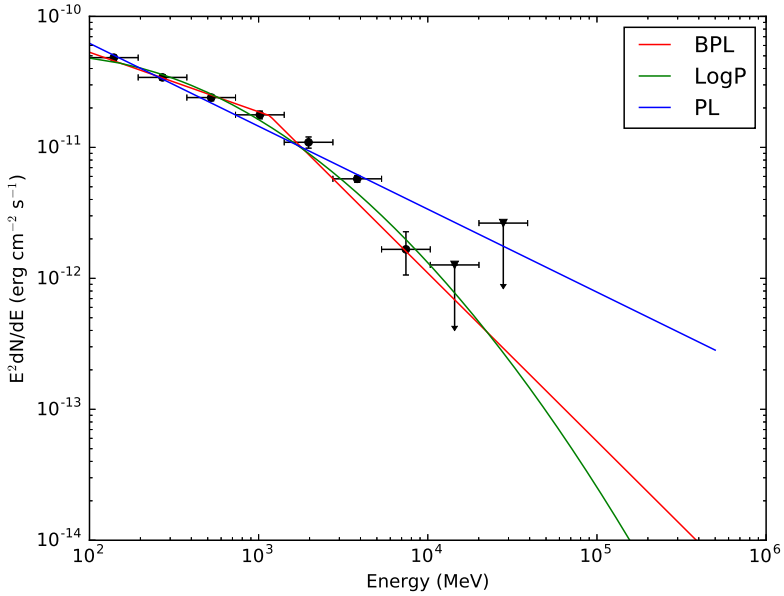

Fig. 5 *Fermi* γ-ray spectrum of 4C 50.11 during the total P2–P6 time interval. The PL, BPL and LogP model fits are shown as *blue*, *red* and *green* curves, respectively.

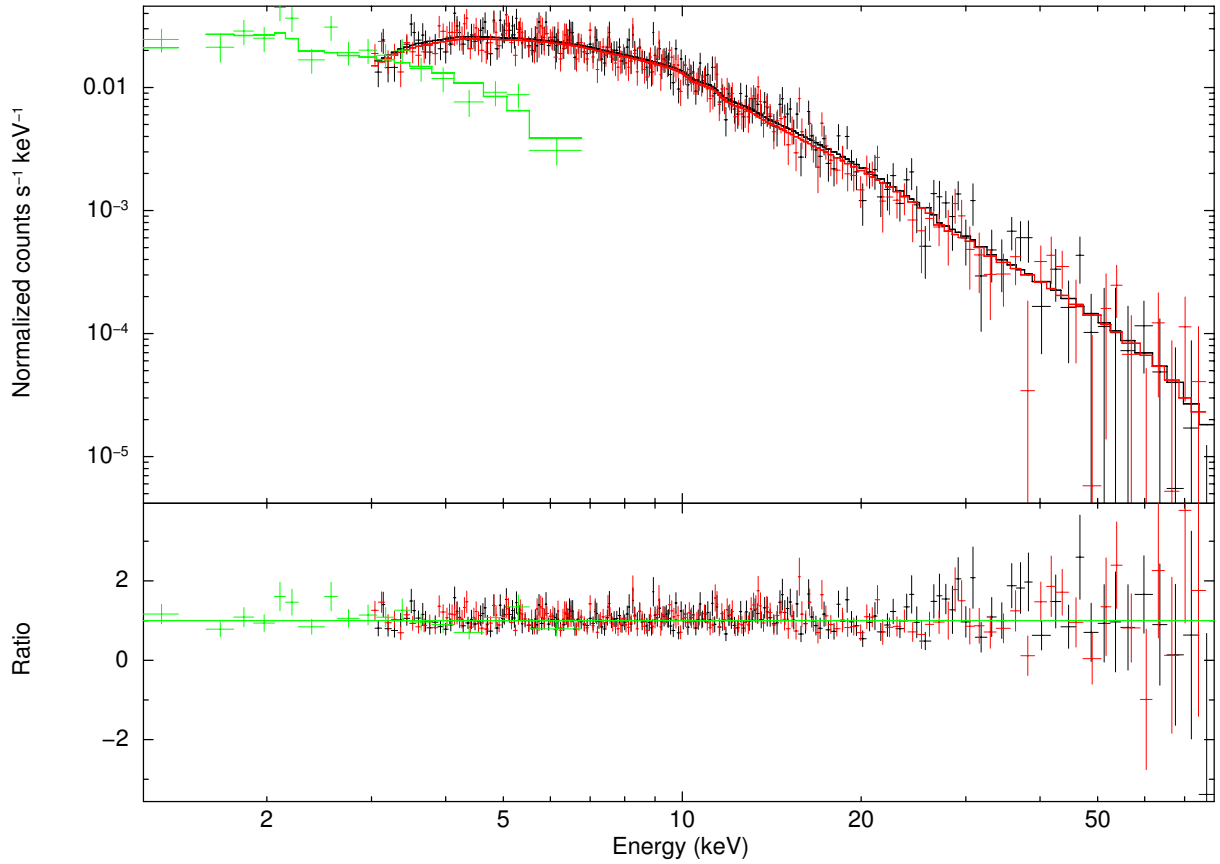

Fig. 6 *NuSTAR* (*red* and *black* points) and *Swift*-XRT (*green* points) spectra and residuals of 4C 50.11, simultaneously fitted with a broken PL.

Table 4 Simultaneous Fit of *NuSTAR* and *Swift*-XRT Data

Model	Parameter	Value
PL	$\Gamma_{\rm X}$	$1.51^{+0.04}_{-0.03}$
	Flux $(0.3-79\,{\rm keV})$	$3.28^{+0.14}_{-0.13}$
	$\chi^2/{\rm d.o.f}$	373.1/407
PL +	$\Gamma_{\rm X}$	1.56 ± 0.05
Extra absorber	$N_{\rm H}^{z}(\times10^{22}\ {\rm cm}^{-2})$	$5.47^{+3.50}_{-3.10}$
	Flux $(0.3-79\,{\rm keV})$	3.21 ± 0.14
	$\chi^2/{\rm d.o.f}$	363.9/406
PL +	$\Gamma_{\rm X}$	$1.63^{+0.09}_{-0.08}$
Exponential	$E_{\rm f}\,({\rm keV})$	$0.87^{+0.60}_{-0.57}$
roll-off	Flux $(0.3-79\,{\rm keV})$	$3.09^{+0.18}_{-0.17}$
	$\chi^2/{\rm d.o.f}$	366.7/406
Broken PL	Γ_1	$0.05^{+0.88}_{-1.71}$
	$E_{\rm break}$	$2.13^{+0.62}_{-0.31}$
	Γ_2	$1.52^{+0.04}_{-0.03}$
	Flux $(0.3-79\,{\rm keV})$	$3.23^{+0.14}_{-0.13}$
	$\chi^2/{\rm d.o.f}$	360.5/405

Notes: The errors are at the 90% confidence level. Flux is in the unit of $10^{-11}\,{\rm erg\,cm^{-2}\,s^{-1}}$ and corrected for absorption.

Our temporal analysis has shown that 4C 50.11 exhibited variability on the timescale of as low as several hours, which is not commonly seen for high redshift blazars. A blazar jet is produced at the central region around the super-massive black hole (BH), and as the inner region cannot be resolved with current telescopes (note that thus far, M87 is the only source that has been resolved with current observing facilities, which reaches several Schwarzschild radii, see Hada et al. 2011), variability is a useful feature for probing this region. Given the variability timescale of 4C 50.11, causality implies that the size of the emission region is $R = t_{\rm var}c\delta/(1+z) = 4.2\times10^{14}(\delta/10)(t_{\rm var}/1\ {\rm h})\ {\rm cm} = 1.36\times10^{15}\,{\rm cm}$ (taking $t_{\rm var}\simeq 4\,{\rm h}$ and $\delta = 7.9$; for the δ value, see below), which is comparable to the Schwarzschild radius. The central BH mass of this source is $\approx 4.68\times10^9\,M_\odot$ and corresponding Schwarzschild radius is $1.38\times10^{15}\,{\rm cm}$ (Acosta-Pulido et al. 2010). Assuming the low-energy X-ray emission is produced from the same region, the γ-ray photons could be absorbed by X-ray photons through the pair production effect. The strength of this absorption is mainly dependent on the X-ray energy density, which will decrease if emission is relativistically Doppler beamed. Therefore, the observed γ-ray and X-ray data can be used to constrain the jet Doppler factor. Because the γ-ray photons actually escape from the emission region, the several-hours timescale constrains the lower limit of the beaming factor, $\delta \geq 11.8[(1\ {\rm h}/t_{\rm var})(1\ {\rm keV}/\epsilon_X)(L_{\epsilon_X}/10^{46}\,{\rm erg\,s^{-1}})]^{1/4}$, where $\epsilon_X E_\gamma = 20.61(\delta/10)^2$ (Dondi & Ghisellini 1995). Considering γ-ray photons with energies of $\sim$1 GeV and the X-ray luminosity of the source obtained in this study, the Doppler beaming factor $\delta \geq 7.9$ ($t_{\rm var}\sim 4\,{\rm h}$). VLBI observations show that the apparent superluminal motion reaches $\beta_{\rm app} = 6.3c$ and the central jet changes direction by about $\sim 100^\circ$ (Agudo et al. 2007; Molina et al. 2014). Combining these with the assumption of $\delta = 7.9$, we have estimated the viewing angle $\theta = 7.9^\circ$ and the bulk Lorentz factor $\Gamma_{\rm bulk} = 6.5$, which suggest that the jet is highly relativistic and has a small viewing angle with respect to our line of sight.

5.2 X-ray Properties

We have investigated the X-ray properties of 4C 50.11 using *Swift*-XRT and *NuSTAR* observations. The source showed variability in the long-term *Swift*-XRT light curve. While its intensity was at the high end of the variation range during the γ-ray flaring period (Fig. 4; only the 2014 February *Swift* observation was conducted in the time period), no significant correlated activity was seen. The X-ray spectral parameters obtained in the active period did not have drastic changes either. We considered that X-rays and γ-rays are produced from the IC scattering radiation by the same electron population. Because the cooling timescale of electrons in the lower energy part (in X-rays) is longer than the timescale of the higher energy part (in γ-rays), one can expect that the X-ray variability timescale would be longer than that of the γ-rays.

Table 5 SED Model Parameters for 4C 50.11

State	B	R	N_0	δ	γ_0	$\gamma_{\rm min}$	p_1	p_2	$P_{\rm jet}^{e-p}$	$P_{\rm jet}^{e-e^+}$	$L_{\rm disk}$
	Gs	(10^{15}cm)							(10^{48} erg s^{-1})	(10^{45} erg s^{-1})	(10^{47} erg s^{-1})
High	0.8	3.80	0.628E+07	22.16	34.80	1.1	2.2	3.3	4.616	5.930	1.8
Low	0.8	4.29	0.422E+07	20.00	30.62	1.1	2.2	3.6	3.203	3.973	1.8

The spectral flattening of the soft X-ray spectrum has been widely found in high-redshift radio loud quasars (e.g. Yuan et al. 2006, and references therein). The flattening may be due to either intrinsic absorption with column densities of the order of $10^{22} - 10^{23}\,{\rm cm}^{-2}$ or low energy cut-off in the energy distribution of electron population in the jet (Fabian et al. 2001b,a; Worsley et al. 2004a,b). In the excess absorption scenario, high $N_{\rm H}^z$ may be dense plasma in the form of a wind or outflow (Fabian 1999). However in radio-loud quasars like 4C 50.11, the relativistic jet along the line-of-sight can remove the gas column efficiently. Indeed, the VLBI observations (Agudo et al. 2007) have revealed a jet toward the Earth, suggesting that the excess absorption scenario is not likely the case.

If there is a low energy cut-off in the energy distribution of the electron population, a spectrum is expected to flatten in the soft energy band (Fabian et al. 2001b; Tavecchio et al. 2007; Sambruna et al. 2007). This scenario requests a broken PL model, where the cut-off in the soft X-ray band can naturally be explained as intrinsic curvature of the spectrum near the low-energy end of the IC component. The soft X-ray flattening is then an intrinsic feature of a source. Among the four examined observations of 4C 50.11, the spectra were relatively well described by the broken PL model of $\Gamma_1 \sim -0.3$ – +0.9 below the break energy $E_{\rm break} = 2.1$ – 3.3 keV, and $\Gamma_2 \sim$1.4–1.8 above the break energy. Simultaneous observations of 4C 50.11 by *Swift* and *NuSTAR* showed that the broad-band X-ray spectrum is better modeled by a broken PL than by a PL or a PL plus extra absorption model. We found $\Gamma_1 = 0.05^{+0.88}_{-1.71}$ below the break energy, $E_{\rm break} = 2.13^{+0.62}_{-0.31}$ keV and $\Gamma_2 = 1.52^{+0.04}_{-0.03}$ above the break energy. In the 14–195 keV energy range of *Swift*-BAT, the source was found to have photon index $\Gamma_{\rm X} = 1.51 \pm 0.35$ (Baumgartner et al. 2013), which is well in agreement with Γ_2 obtained in our broad-band fit. Thus we suspect that the flattening is likely the intrinsic feature of the source. This possibility is supported by the broad-band SED modeling (see the following Sect. 5.3 and Table 5). From the modeling, it can be known that the low energy of non-thermal electrons is about $\gamma_{\rm min} \sim 1.1$ and the Doppler beaming factor $\delta \sim 22.5$ for the active state. Electrons around the minimum energy will IC scatter external seed photons, and emit at $\nu_{\rm IC} \approx (4/3)\delta\Gamma_{\rm jet}\gamma_{\rm min}^2\nu_{\rm ext}/(1+z) \sim 2.6$ keV (assuming $\Gamma_{\rm jet} = \delta$), which is roughly consistent with observations (similarly, we have $\nu_{\rm IC} \approx 2.1$ keV for the quiescent state).

5.3 Spectral Energy Distribution Fitting

We collected the archival radio and optical data for 4C 50.11 from Acosta-Pulido et al. (2010) and NED[2] respectively. These data were combined with X-ray and γ-ray data in this work and the broad-band SED of the source is shown in Figure 7. In this SED, emission from the relativistic jet dominated except at optical wavelengths. The optical emission reached a peak luminosity of $\sim 10^{47}$ erg s^{-1} and appeared as a significant bump, which should be thermal, arising from the optically thick accretion disk. As 4C 50.11 hosts a very massive BH, the thermal disk emission reaches $\sim 30\%$ of the Eddington limit (Acosta-Pulido et al. 2010). The broad-band SED is not simultaneous, except for the two sets of *Swift* X-ray and the corresponding *Fermi* γ-ray data in the active and quiescent states (the red and blue squares, respectively, in Fig. 7). Nevertheless, we modeled the broad-band SED by using a standard blazar emission model: one zone synchrotron plus inverse Comptonization model. This model was widely used in blazar SED modeling (e.g., Ghisellini et al. 2010; Chen et al. 2012; Chen 2017). The emission region is assumed to be a homogeneous sphere with radius R embedded in the magnetic field B. A broken PL electron energy distribution,

$$N(\gamma) = \begin{cases} N_0\gamma^{-p_1} & \gamma_{\rm min} \le \gamma \le \gamma_0, \\ N_0\gamma_0^{p_2-p_1}\gamma^{-p_2} & \gamma_0 < \gamma \le \gamma_{\rm max}, \end{cases} \quad (2)$$

was assumed in our calculation. The parameters of this model include radius R of the blob, magnetic field strength B, electron break energy γ_0, the minimum and

[2] *http://ned.ipac.caltech.edu/*

maximum energy, $\gamma_{\rm min}$ and $\gamma_{\rm max}$ respectively, of the electrons, normalization of the particle number density N_0, and indices $p_{1,2}$ of the broken PL particle distribution, jet Doppler factor (assumed to be equal to the bulk Lorentz factor), and spectrum of the external seed photons. The frequency and luminosity can be transformed from the jet frame to observational frame as

$$\nu = \delta\nu'/(1+z) \quad \text{and} \quad \nu L_\nu = \delta^4 \nu' L'_{\nu'},$$

where the Doppler factor $\delta = 1/\left[\Gamma\left(1-\beta\cos\theta\right)\right]$, and prime represents the value measured in the jet frame. The synchrotron self-absorption and the Klein-Nishina effect in the IC scattering were properly considered in our calculations. Both self-synchrotron Compton (SSC) scattering and external Compton (EC) scattering (external seed photons from the BLR and dusty torus were taken into account) were included in calculation of the Compton scattering in the blob.

As mentioned above, the optical emission is multi-temperature annular blackbody radiation arising from the accretion disk, which was modeled with a standard optically thick, geometrically thin disk (Shakura & Sunyaev 1973). Above the accretion disk, the corona reprocessed a fraction of disk luminosity (fixed at a level of 10%) and had a PL spectrum with cut-off energy 150 keV (we fixed the spectral index $\alpha = 1.0$). Because the accretion disk's radiation is de-beamed in the jet comoving frame, seed photons from it were not important and thus not included in the EC scattering. In our SED modeling, the luminosities of the BLR and dust torus were assumed to be a fraction of the disk luminosity, 10% and 50% respectively (Ghisellini & Tavecchio 2008). The radii of the BLR and torus were $R_{\rm BLR}= 10^{17} L_{\rm disk,45}^{1/2} = 0.43\,{\rm pc}$ and $R_{\rm torus} = 2.5\times10^{18} L_{\rm disk,45}^{1/2} = 10.9\,{\rm pc}$, respectively ($L_{\rm disk,45} = 179.0$ is the disk luminosity in units of $10^{45}\,{\rm erg\,s^{-1}}$; see Acosta-Pulido et al. 2010). In this case, the external photon energy densities are typical values $U_{\rm BLR}= 2.65\times10^{-2}\,{\rm erg\,cm^{-3}}$ and $U_{\rm torus} = 2.12\times10^{-4}\,{\rm erg\,cm^{-3}}$. The size of the emitting region was assumed to be equal to the radius of a circular conic section, $R = \psi R_{\rm diss}$ ($R_{\rm diss}$ is the distance of the emission region from the central BH, where $\psi = 0.1$; see Ghisellini & Tavecchio 2008). The variability timescale can be used to set an upper limit on the emission size due to causality, $R \lessapprox c\Delta t\delta/(1+z)$. During our SED modeling, the minimum variability timescale ($\Delta t \approx 4\,{\rm h}$) was used for estimating the size of the emission region for the active state. Note that the Doppler factor estimated in Section 5.1, $\delta \gtrsim 7.9$, was the lower limit to avoid absorption of γ-ray photons through the electron pair production effect.

In Figure 7, we show model fits to the SEDs in both active and quiescent states, with seed photons dominantly coming from the BLR. The model parameters are given in Table 5. From the jet bolometric luminosity $L_{\rm jet}$, we can obtain the jet non-thermal radiation power (Ghisellini et al. 2014), $P_{\rm rad} \approx 2L_{\rm tot}/\delta^2 = 3.1\times10^{46}$ erg s^{-1} for the active state, which is about 17% of the disk luminosity of 1.8×10^{47} erg s^{-1}. The jet radiative efficiency is believed to be on the order of $P_{\rm rad}/P_{\rm jet}$ ~10%, which holds for AGNs, gamma-ray bursts, and even for BH X-ray binaries (Nemmen et al. 2012; Zhang et al. 2013; Ma et al. 2014). This gives a jet power, $P_{\rm jet} \approx 10P_{\rm rad} = 3.1\times10^{47}$ erg s^{-1}, larger than the disk luminosity, suggesting that the jet launching processes and the way of transporting energy from the vicinity of the BH must be very efficient. Actually, having the model parameters, the jet power can be calculated as $P_{\rm jet} \simeq \pi R^2\beta\Gamma^2 cU'_{\rm tot}$, where the total energy density, measured in the rest frame of the jet, $U'_{\rm tot} = U'_{\rm e} + U'_{\rm B} + U'_{\rm p}$. The energy density for electrons $U'_{\rm e} = m_{\rm e}c^2\int N(\gamma)\gamma d\gamma$, while the proton energy density $U'_{\rm p} = U'_{\rm e}(m_{\rm p}/m_{\rm e})/\langle\gamma\rangle$ if charge neutrality for pure hydrogen plasma is assumed. The estimated values for the jet powers are given in Table 5. It can be seen that the jet power $P_{\rm jet}$ is larger than the disk luminosity $L_{\rm disk}$ by more than one magnitude and even larger than that of accretion power

$$P_{\rm acc} = L_{\rm disk}/\eta \approx (0.6-1.8)\times10^{48}\,{\rm erg\,s^{-1}},$$

where the radiative efficiency of the accretion disk is assumed to be $\eta \approx 0.1-0.3$ (Ghisellini et al. 2014). However, we note that the minimum electron energy in our fitting is small, $\gamma_{\rm min} = 1.1$ (Table 5). The small value of $\gamma_{\rm min}$ may result in overestimation of the jet power. In SED modeling, the reproduction of X-ray emission is important for constraining $\gamma_{\rm min}$. In Zhang et al. (2014, 2015), X-ray is produced through SSC mechanism, in which $\gamma_{\rm min}$ is much larger than the unit ($\gamma_{\rm min} \gg 1$). In our SED modeling, we failed to model the X-ray with SSC emission; instead, following Ghisellini et al. (1998, 2010), we modeled the X-ray through EC emission and therefore obtained a small $\gamma_{\rm min}$ (similar to Ghisellini et al. 1998, 2010). In addition, it should be noted that the estimated jet power is largely dependent on the assumed jet components. For example, if the jet is mainly

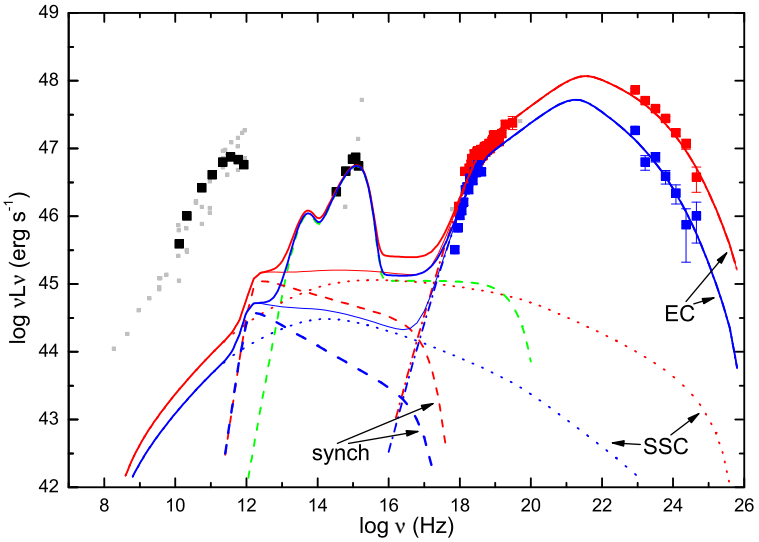

Fig. 7 Broad-band SED of 4C 50.11, where the *black* and *grey* data points are respectively from Acosta-Pulido et al. (2010) and NED. The *red* points (lines) stand for active states, while the *blue* ones for quiescent states. *Solid lines* are for the EC/BLR model. The central accretion disk/corona/dust torus emission component is represented using a *green dashed line*. The *red/blue dashed*, *dotted* and *dash-dotted* lines are synchrotron, SSC and EC emissions in active/quiescent states, respectively.

composed of electron-positron pairs instead of electron-proton plasma, the jet powers will be significantly decreased and smaller than the accretion disk luminosity for both active and quiescent states (see Table 5).

6 SUMMARY

We have studied γ-ray and X-ray properties of the high redshift blazar 4C 50.11 by analyzing the *Fermi*-LAT, *Swift* and *NuSTAR* data. The main results are summarized as follows:

(1) From *Fermi*-LAT monitoring, the source was found to be in an active state since approximately MJD 56482. During the state, the source's γ-ray flux increased as largely as nearly one order of magnitude (averaged over 5 d bins) compared to the quiescent level. In addition, the γ-ray spectra appeared harder during the active period. We also found that the γ-ray variability can be resolved on the level of several hours. This property has helped to constrain the physical properties of the jet associated with the blazar.

(2) The source showed flux variability in the *Swift* and *NuSTAR* data we have analyzed, but no obvious flux enhancement or spectral changes related to the γ-ray active state were seen. As long as the data quality allows, we have found that a broken PL provided the best fit to the broad-band X-ray spectra, with an extremely flat spectrum ($\Gamma \sim 0.1$) below the break energy, $E_{\rm break} \sim 2.1\,{\rm keV}$, and a flat spectrum above the break energy. This spectral feature is likely due to the low-energy cutoff in the energy distribution of the photon-emitting electron population.

(3) We have constructed the broad-band SED for 4C 50.11, though not simultaneously, and provided a model fit (one-zone synchrotron plus inverse Comptonization model) to the SED. From modeling, properties of the emission region were derived.

Acknowledgements We acknowledge the use of data from *Fermi* Science Support Center (FSSC), and *Swift* and *NuSTAR* data from the High Energy Astrophysics Science Archive Research Center (HEASARC), at NASA's Goddard Space Flight Center. This research has made use of the High Performance Computing Resource in the Core Facility for Advanced Research Computing at Shanghai Astronomical Observatory, and the *NuSTAR* Data Analysis Software (NUSTARDAS) jointly developed by the ASI Science Data Center (ASDC, Italy) and the California Institute of Technology (Caltech, USA).

This research was supported by the National Program on Key Research and Development Project (Grant No. 2016YFA0400804), the National Natural Science Foundation of China for Youth (11603059), the National Natural Science Foundation of China (11373055, 11633007, 11233006 and U1431123), and the CAS grant (QYZDJ-SSW- SYS023). VJ

acknowledges financial support from Chinese Academy of Sciences through the President's International Fellowship Initiative (CAS PIFI, Grant No. 2015PM059). Z.W. acknowledges support by the CAS/SAFEA International Partnership Program for Creative Research Teams.

References

Abdo, A. A., Ackermann, M., Agudo, I., et al. 2010a, ApJ, 721, 1425
Abdo, A. A., Ackermann, M., Ajello, M., et al. 2010b, ApJ, 722, 1303
Abdo, A. A., Ackermann, M., Ajello, M., et al. 2010c, ApJ, 722, 520
Abdo, A. A., Ackermann, M., Ajello, M., et al. 2011a, ApJ, 736, L11
Abdo, A. A., Ackermann, M., Ajello, M., et al. 2011b, ApJ, 733, L26
Abdo, A. A., Ajello, M., Allafort, A., et al. 2013, ApJS, 208, 17
Acero, F., Ackermann, M., Ajello, M., et al. 2015, ApJS, 218, 23
Ackermann, M., Ajello, M., Atwood, W. B., et al. 2015, ApJ, 810, 14
Acosta-Pulido, J. A., Agudo, I., Barrena, R., et al. 2010, A&A, 519, A5
Agudo, I., Thum, C., Wiesemeyer, H., & Krichbaum, T. P. 2010, ApJS, 189, 1
Agudo, I., Bach, U., Krichbaum, T. P., et al. 2007, A&A, 476, L17
Agudo, I., Bach, U., Krichbaum, T. P., et al. 2008, in ASPC Series, 386, Extragalactic Jets: Theory and Observation from Radio to Gamma Ray, eds. T. A. Rector, & D. S. De Young, 249
Band, D. L., & Grindlay, J. E. 1985, ApJ, 298, 128
Barthelmy, S. D., Barbier, L. M., Cummings, J. R., et al. 2005, Space Sci. Rev., 120, 143
Baumgartner, W. H., Tueller, J., Markwardt, C. B., et al. 2013, ApJS, 207, 19
Blandford, R. D., & Rees, M. J. 1978, in BL Lac Objects, ed. A. M. Wolfe, 328
Błażejowski, M., Sikora, M., Moderski, R., & Madejski, G. M. 2000, ApJ, 545, 107
Burrows, D. N., Hill, J. E., Nousek, J. A., et al. 2005, Space Sci. Rev., 120, 165
Carpenter, B., Ojha, R., D'Ammando, F., Orienti, M., & Cheung, C. C. 2014, The Astronomer's Telegram, 5838
Cash, W. 1979, ApJ, 228, 939
Chen, L. 2017, ApJ, 842, 129
Chen, L., Cao, X., & Bai, J. M. 2012, ApJ, 748, 119
Dondi, L., & Ghisellini, G. 1995, MNRAS, 273, 583
Fabian, A. C. 1999, MNRAS, 308, L39
Fabian, A. C., Celotti, A., Iwasawa, K., & Ghisellini, G. 2001a, MNRAS, 324, 628
Fabian, A. C., Celotti, A., Iwasawa, K., et al. 2001b, MNRAS, 323, 373
Fey, A. L., Ma, C., Arias, E. F., et al. 2004, AJ, 127, 3587
Foschini, L. 2009, Advances in Space Research, 43, 1036
Foschini, L. 2010, The Astronomer's Telegram, 2517
Foschini, L., Bonnoli, G., Ghisellini, G., et al. 2013, A&A, 555, A138
Gehrels, N., Chincarini, G., Giommi, P., et al. 2004, ApJ, 611, 1005
Ghisellini, G., Celotti, A., Fossati, G., Maraschi, L., & Comastri, A. 1998, MNRAS, 301, 451
Ghisellini, G., & Tavecchio, F. 2008, MNRAS, 387, 1669
Ghisellini, G., Tavecchio, F., Foschini, L., et al. 2010, MNRAS, 402, 497
Ghisellini, G., Tavecchio, F., Maraschi, L., Celotti, A., & Sbarrato, T. 2014, Nature, 515, 376
Hada, K., Doi, A., Kino, M., et al. 2011, Nature, 477, 185
Harrison, F. A., Craig, W. W., Christensen, F. E., et al. 2013, ApJ, 770, 103
Hayashida, M., Nalewajko, K., Madejski, G. M., et al. 2015, ApJ, 807, 79
Kalberla, P. M. W., Burton, W. B., Hartmann, D., et al. 2005, A&A, 440, 775
Konigl, A. 1981, ApJ, 243, 700
Krauss, F., Carpenter, B., Ojha, R., Kadler, M., & Wilms, J. 2014, The Astronomer's Telegram, 5878
Ma, R., Xie, F.-G., & Hou, S. 2014, ApJ, 780, L14
Maraschi, L., Ghisellini, G., & Celotti, A. 1992, ApJ, 397, L5
Molina, S. N., Agudo, I., Gómez, J. L., et al. 2014, A&A, 566, A26
Nemmen, R. S., Georganopoulos, M., Guiriec, S., et al. 2012, Science, 338, 1445
Pauliny-Toth, I. I. K., Wade, C. M., & Heeschen, D. S. 1966, ApJS, 13, 65
Sambruna, R. M., Tavecchio, F., Ghisellini, G., et al. 2007, ApJ, 669, 884
Scarpa, R., & Falomo, R. 1997, A&A, 325, 109
Tavecchio, F., Maraschi, L., Ghisellini, G., et al. 2007, ApJ, 665, 980
Urry, C. M., & Padovani, P. 1995, PASP, 107, 803
Wilms, J., Allen, A., & McCray, R. 2000, ApJ, 542, 914
Worsley, M. A., Fabian, A. C., Celotti, A., & Iwasawa, K. 2004a, MNRAS, 350, L67
Worsley, M. A., Fabian, A. C., Turner, A. K., Celotti, A., & Iwasawa, K. 2004b, MNRAS, 350, 207
Yuan, W., Fabian, A. C., Worsley, M. A., & McMahon, R. G. 2006, MNRAS, 368, 985
Zhang, J., Liang, E.-W., Sun, X.-N., et al. 2013, ApJ, 774, L5
Zhang, J., Sun, X.-N., Liang, E.-W., et al. 2014, ApJ, 788, 104
Zhang, J., Xue, Z.-W., He, J.-J., Liang, E.-W., & Zhang, S.-N. 2015, ApJ, 807, 51